Chinese Chemical Letters 35 (2024) 108705

Contents lists available at ScienceDirect

Chinese Chemical Letters

journal homepage: www.elsevier.com/locate/cclet

Versatile oxidized variants derived from TMDs by various oxidation strategies and their applications

Gu Gong, Mengzhu Li, Ning Sun, Ting Zhi*, Yuhao He, Junan Pan, Yuntao Cai, Longlu Wang*

College of Electronic and Optical Engineering & College of Flexible Electronics (Future Technology), Nanjing University of Posts & Telecommunications (NUPT), Nanjing 210023, China

ARTICLE INFO

Article history:
Received 1 May 2023
Revised 26 May 2023
Accepted 19 June 2023
Available online 21 June 2023

Keywords:
Transition metal dichalcogenides
Oxidation strategies
Oxidized variants
Hydrogen evolution reaction
Physicochemical properties

ABSTRACT

The physicochemical properties of transition metal dichalcogenides (TMDs) are highly related to their structures and usually stable in air. However, under certain conditions they could be transformed into different structures due to oxidation. Considering this, various materials with fascinating structures have been explored by oxidation strategies, which possess novel properties and great potential in various applications such as solar batteries, hydrogen evolution reaction (HER) catalysts, and field effect transistors (FET). In this review, we systematically summarize the atomic structures of TMD oxidized variants and the corresponding fabrication approaches. Utilizing various characterization methods, the chemical components of TMD oxidized variants are illustrated. Furthermore, we expound the promising applications of the oxidized variants. This review is expected to provide a new insight for preparing precise materials at the atomic level through corresponding oxidation strategies.

1. Introduction

Transition metal dichalcogenides with the chemical formula MX_2 (M: transition metal element; X: chalcogen) are binary layered compounds with hexagonal lattice structure, where the atoms are bound in the form of M-X bonds in the basal plane and the MX_2 layer is combined with the adjacent layer by van der Waals force [1–4]. Considering its excellent optical [5–7], electrical [8–12], magnetic [13–16], mechanical [17,18] and thermal properties [19–24], it is emerged as a splendid material utilized in energy storage [25–27], catalysis [28–30], semiconductor [31–35], lubrication [36,37] and other fields. For example, if we fabricate flexible electrodes for hydrogen evolution reaction (HER) with transition metal dichalcogenides (TMDs), the mechanical stability of the catalytic system can be enhanced due to the excellent mechanical properties can make the catalyst resist the stress caused by the stretching and rupture of bubbles in the high-current catalytic reaction [38]. The TMDs exist widely in nature, and most of them are air-stable [39–41]. However, considering the defects of primitive TMDs, including inert basal plane and limited electronic transmission efficiency, it is urgent to find effective regulating strategies of MX_2 to develop more potential applications. Fortunately, due to the intrinsic relationship between specific physicochemical properties and atomic structures, the properties and application fields of TMDs can be expanded by chemical modification.

Oxide modification is an effective method to transform the physicochemical properties of TMDs. In this way, a large material system can be formed, such as variants without changes of intrinsic elements, variants with single oxygen atom doping, heterojunction, and dioxides with interlayered elementary substance. It had been reported that various synthetic strategies, including spontaneous oxidation [42–44], high temperature thermal annealing [45–49], H_2O_2 etching [50–52], electrochemical oxidation [53–56], oxygen plasma treatment [57–60], ultraviolet-ozone (UV-O_3) treatment [61,62], and laser treatment [63–65], were used to treat MX_2 to acquire special oxidized variants with precise atomic structures. For example, Huang *et al.* [66] prepared the atomic structure of oxidized ReS_2 by UV-O_3 treatment. In their research, except the *in-situ* oxidation of S atoms, there exist exotic covalently-bonded surface oxygen atoms which distort the atomic structure of single-layer (1 L) ReS_2 slightly. In this way, two of the four crystallographically distinct S atoms in the same unit cell having the bonding lengths which are much is oxygen atop sulfur and the other is substitutional oxygen on the sulfur vacancy (SV). Besides, Tan *et al.* [67] reported that they fabricated $MoS_{2-x}O_x$ nanosheets and get the diverse oxygen incorporation extent of $MoS_{2-x}O_x$. Due to

* Corresponding authors.
E-mail addresses: Zhit@njupt.edu.cn (T. Zhi), wanglonglu@njupt.edu.cn (L. Wang).

https://doi.org/10.1016/j.cclet.2023.108705
1001-8417/

the enhancement of intrinsic conductivity and the acceleration of the interfacial charge transfer after oxygen doping, the $MoS_{2-x}O_x$ demonstrated a remarkable degradation activity for antibiotics. The $MoS_{2-x}O_x$ would dramatically boost the degradation activity of persistent contaminants in the co-catalyst Fenton system, which provides a new method for higher environmental decontamination performance. These studies above have proved that specific oxidation products can be obtained on demand through certain oxidation strategies. However, the recent researches are not sufficient and needs to be summarized systematically.

In this review, we firstly summarize the atomic structures of TMD oxidized variants. What is more, the mechanisms for corresponding fabrication approaches are provided. Since MoS_2 is a typical kind of TMDs and its oxidation structure has been widely studied in recent years, and TMDs often have similar physical and chemical properties. Based on the researches of MoS_2, the properties of other kinds of oxidation variants of TMDs will be described afterwards. In the end, we provide the outlooks of future applications of the TMD oxidized variants. This review is expected to establish the material system of the TMD oxidized variants, aiming to provide insight into the design potential application of TMD oxidized variants.

2. Oxidized variants without changes of intrinsic elements

As we all know, the oxidation process could change the atomic structure of TMDs by forming or breaking chemical bonds. In some cases, the oxidation process only changes the atomic structure, such as forming thinner stacked layers and triangular pits, without introducing new types of elements. The generation of these new structures would bring some novel physicochemical properties and have potential application values.

2.1. Stacked few-layer (bi/tri-layer) structure

Transition metal dichalcogenides has the structures featured by stacking layers. Recently, various of preparation researches are reported in order to obtain single or few layers of TMDs [68–71]. Among them, electrochemical oxidation exfoliation is an excellent way which converts multiple layers of TMDs into single layers by partially oxidizing TMDs in an electrochemical environment and the oxidized parts dissolve into the solution.

Pan *et al.* [72] reported an electrochemical exfoliation method for stacked few-layer (bi/tri-layer) MoS_2 driven by a lateral inward electrochemical reaction (Fig. 1A). In this electrochemical reaction, water molecules go into interlayered space through the formed two-dimension (2D) channel. Then, the bulk MoS_2 could be electrochemically selectively oxidized and finally the remaining bi/tri-layer MoS_2 forms a stacked structure. By this means, the interlayered MoS_2 reacts as the function: $MoS_2 + 8H_2O \rightarrow Mo^{6+} + 2SO_4{}^{2-} + 16H^+ + 18e^-$ with the high anodic potential applied to bulk MoS_2 in the solution of sulfate electrolyte. The atomic structure is shown in Fig. 1B, the edge of MoS_2 is etched selectively with the 2D channel created subsequently, leaving a stacked structure in the form of uniform bi/tri-layer MoS_2 layers, which made the remaining MoS_2 layers restacked together with a decreased thickness. This phenomenon results from the oxidation of MoS_2 to Mo^{6+} and the dissolution of oxidized MoS_2 in the sulfate electrolyte. The scanning transmission electron microscope (STEM) image (Fig. 1C) proves the formation of this structure: The most part of multilayer MoS_2 get to a decreased thickness. Meanwhile, the bottom part remains the original thickness due to the strong Coulomb interaction between substrate and bottom MoS_2 which inhibits electrochemical reaction. The special atomic structure distinguishes the electrochemical exfoliation from traditional corrosion and etching methods.

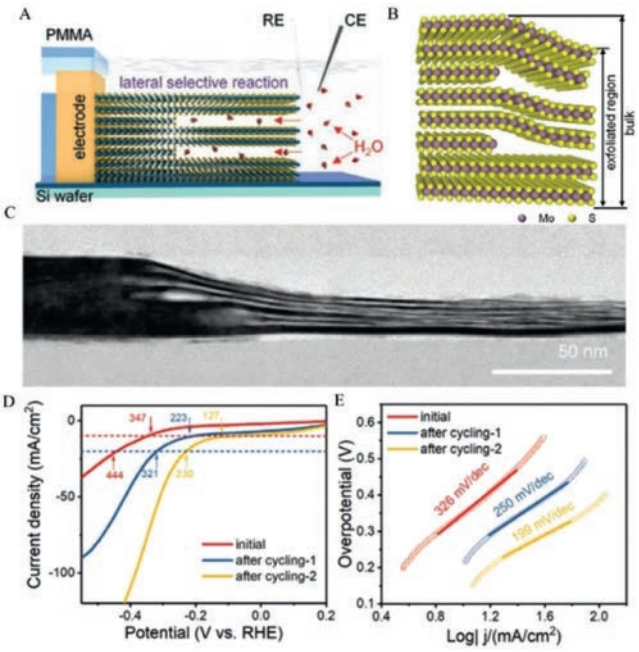

Fig. 1. (A) The schematic of the process driven by a lateral inward electrochemical reaction and water molecules go into bulk phase through the formed 2D channel. (B) The schematic of the thickness of the edge and the basal plane of MoS_2 after exfoliation. (C) The magnified STEM image of the transition zone from bulk to edge. (D) The polarization curves of MoS_2 after different CV cycles treatment (0, 200, and 300 cycles). The dash lines mark the overpotential at 10 and 20 mA/cm^2. (E) The corresponding Tafel slope plots. Reproduced with permission [72]. Copyright 2021, John Wiley & Sons, Ltd.

Interestingly, in the process of electrochemical exfoliation, adding some steps can make the product have more properties. In the research of Yu *et al.* [73], during electrochemical exfoliation of ReS_2, they use large sized molecular intercalants to induce parallel mirror twin boundaries and atomic row dislocation. Through the calculation *via* density function theory (DFT), they conclude that ferromagnetism is detected due to the combined effects of lattice strain and SVs in the mirror twin boundaries. Meanwhile, the emergence of SVs also enhances the chemical activity of ReS_2 as HER catalysts.

It is worth noting that electrochemical exfoliation is usually a way to reduce the layer of transition metal chalcogenides. To achieve the above experimental phenomenon, it is necessary to accurately control the partial oxidation between TMD layers. Leong *et al.* [74] reported that through electrochemical exfoliation with bipolar electrodes, they successfully made WS_2 undergo a phase transition from 2H to 1T, and reduced the multilayer WS_2 to fewer layers. The electrocatalytic performances of WS_2 is also enhanced. Compared with the phenomenon mentioned above, they realize the complete oxidation of interlayered TMD without forming the stacked structure.

According to the more moderate hydrogen adsorption energy on the sites at edge, this stacked few-layer structure is considered to have an improved HER performance. The exfoliated stacked MoS_2 is applied as catalyst for HER. The polarization curves (Fig. 1D) of the single MoS_2 nanosheet after different CV cycles treatment are recorded in H_2SO_4 based on-chip MoS_2 device. As the bulk MoS_2 electrochemically exfoliated to the stacked bi/tri-layered structure, the overpotential decreases from 347 mV to 127 mV at 10 mA/cm^2. Meanwhile, the Tafel slope (Fig. 1E) decreases from 326 mV/dec to 199 mV/dec. Taking the charge injection from electrode into account, the electrons in bulk MoS_2 transport in the vertical direction through hopping. A $\approx$ 0.12 eV gap for electron hop-

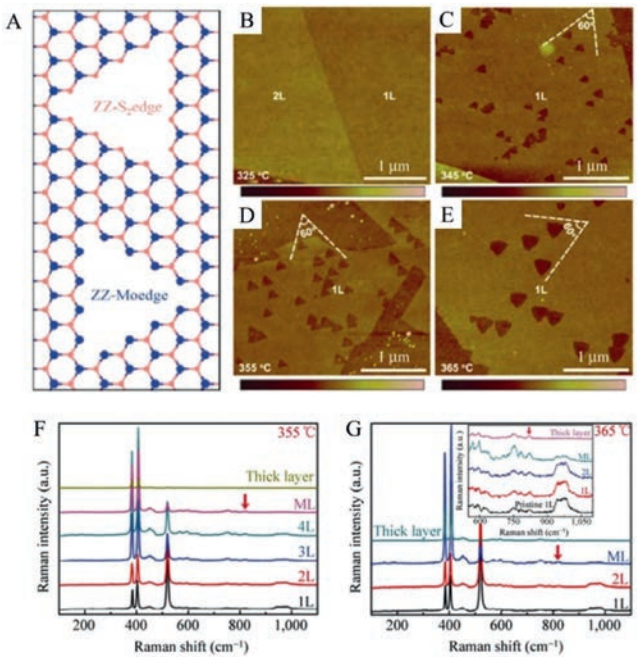

Fig. 2. (A) An atomic mechanism showing the formation of triangular pits in MoS_2 layers. A pit in MoS_2 could generally expose various types of edges, including ZZ-Mo and ZZ-S_2. Typical AFM images showing the formation of well oriented equilateral triangular pits on 1 L MoS_2 at various temperatures: (B) 325 °C, (C) 345 °C, (D) 355 °C, and (E) 365 °C. Raman spectra of n-layer MoS_2 sheets after oxidative etching at (F) 355 °C and (G) 365 °C. Reproduced with permission [77]. Copyright 2013, Tsinghua University Press.

ping is formed by the large van der Waals gap. The potential gap for interlayered electron transfer is reduced by the decreased thickness of MoS_2, which enhances HER performance. Furthermore, the expanded edge sites which have few atomic layers inspire more available active sites. Simultaneously, the reduced thickness enhances the hydrogen adsorption energy. Thus, the novel structure of bi/tri-layer MoS_2 fabricated by electrochemical exfoliation without introducing extra elements would have potential applications in the field of HER.

2.2. TMDs with triangular pits

Some types of TMD oxide would volatilize easily at high temperature [75,76]. In view of this, a special atomic structure of TMDs with triangular pits could be formed through heating TMDs in the absence of air intervention. The formation of such pits is due to the anisotropic oxidation of the TMD edges.

Zhou *et al.* [77] reported the atomic structure of oxidative etching of MoS_2 layers by using a dry oxygen etching reaction where the mechanically exfoliated MoS_2 samples are heated in the center of a tubular furnace with precise modulation at the temperature between 250 °C and 385 °C without the introduction of carrier or reactive gas. As the figure of MoS_2 atomic structure shown in Fig. 2A, the triangular pits are initiated on MoS_2 layer at natural surface defects of MoS_2. The sizes of triangular pits are attributed to the thickness of MoS_2 layers where the 1 L MoS_2 has the smallest pit sizes. As the heating temperature grows, the pits forming due to the anisotropic oxidation of edges of MoS_2 and the Mo and S atoms are transformed to MoO_3 and SO_2 gas molecules respectively, leaving the oxidized MoS_2 with special ratio of basal plane sites to edge sites. Moreover, the typical atomic force microscope (AFM) images of MoS_2 heated in various temperature (Figs. 2B–E) clarified that the etching process increases with the surrounding temperature grows and the angles of triangular pits are close to 60°. When the surrounding temperature is at 325 °C, almost no etching is detected by AFM. However, at 345, 355 and 365 °C, it is easy to find the triangular pits in AFM images and the sides become longer as the temperature grows. Notably, as the temperature increases, the regular triangular pits distort which may attribute to the harsh oxidative etching rate. Lv *et al.* [78] also fabricated the MoS_2 flakes with triangular pits. They heated up the sample in the chemical vapor deposition (CVD) furnace to 300 °C in 10 min, and the sample was etched for 5 min. They also reported no production of MoO_x during the process. Furthermore, they proved that similar oxidation process could be performed on other TMDs, such as $MoSe_2$ and WS_2.

The Raman spectra of MoS_2 sample heated at 355 (Fig. 2F) and 365 °C (Fig. 2G) illustrate that after heating the MoS_2 sample shows the very similar signal with the pristine MoS_2. Although the weak Raman peak shows at ~820 cm^{-1} by red arrows, considering its appearance in the pristine sample, it could not indicate the existence of MoO_3. In short, the TMDs with triangular pits have the enhanced surface properties attributing to the changes of the ratio of edge sites to basal plane sites, which could be utilized as hydrodesulfurization (HDS) or HER catalysts.

3. Oxidized variants with single oxygen atom doping

The oxygen doping is a special kind of oxidation, which mainly embodies in two specific forms of expression: One is the oxygen incorporation of intrinsic SVs generated by artificial synthesis, for example, CVD [79–81]. The other is the oxygen atom bound up atop sulfur atoms, forming new S-O chemical bonds.

3.1. TMDs with oxygen incorporated into SVs

The oxygen incorporation of intrinsic SVs could be realized by many methods, including spontaneous oxidation [82], oxygen plasma treatment [83], electrochemical oxidation [84], *etc.* Although the approaches vary from one to another, the fundamental mechanism remains the same where the oxidation process should be limited in avoid of the complete oxidation of TMDs into trioxide.

3.1.1. Fabricated by spontaneous oxidation

Pető *et al.* [85] fabricate 1 L $MoS_{2-x}O_x$ through spontaneous oxidation, and the structure diagram is exhibited as Fig. 3A, and atomic-resolution STM images which show the basal plane of a mechanically exfoliated 1 L MoS_2 after one month of exposure in air are shown in Fig. 3B. The fresh 2D MoS_2 crystals prepared had natural spot defect density ranging from 1×10^{11} cm^{-2} to 1×10^{12} cm^{-2}. After ambient exposure for 1 month, the spot defect density increased to $3 \times 10^{12} \sim 2 \times 10^{13}$ cm^{-2}. Considering that such abundant area of MoS_2 basal plane distributes defects, it clearly provides evidence for the establishment of new defect sites in MoS_2 under air conditions. Among the species present under ambient conditions, O is predicted to be the most possible to saturate an S vacancy. STM has been shown to be a slow O substitution reaction. When an S atom is replaced by an O atom, it changes the chemical activity of its neighbors, making them more susceptible to being replaced by O atoms, so individual S atoms are replaced by O atoms one by one, in a sort of chain reaction.

In summary, we had drawn the observation that the 1 L MoS_2 has the chance to be oxidized in the air. However, the thermodynamic and dynamical processes of MoS_2 oxidation are in need of expounding. As illustrated in Fig. 3C, the surface S atoms reacts with oxygen, yielding SO_2 and forming the SV in the basal plane. The enthalpy was calculated by the formula $\Delta E = E(\text{reactants}) - E(\text{products}) = -0.49$ eV, which implied that the

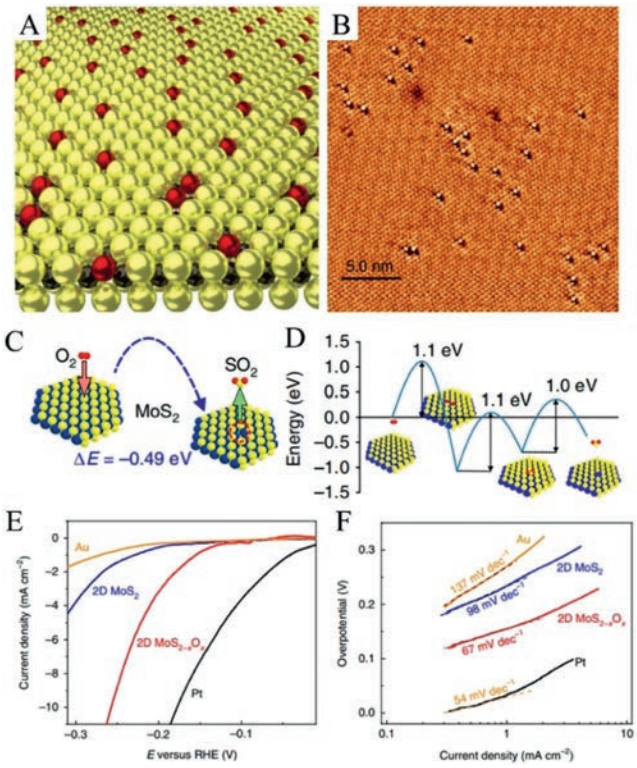

Fig. 3. (A) Schematic atomic structure of the $MoS_{2-x}O_x$ solid solution monolayer. (B) Atomic-resolution STM images (5 mV, 2 nA) of an exfoliated MoS_2 single layer after 1 month. (C) The process of chalcogenide atom vacancy formation through oxidation is characterized by a negative oxidation enthalpy (ΔE) for the defect-free 2D MoS_2 basal plane. (D) Kinetic energy barriers calculated by the NEB model for 2D MoS_2 crystals reveal substantially lower barriers for MoS_2 of ~1 eV height that can be overcome even at room temperature on a months-long timescale. (E) Linear sweep voltammogram curves and (F) corresponding Tafel plotsfor Au substrate, MoS_2 single layer, $MoS_{2-x}O_x$ single layer (1 year old) and Pt substrate. Reproduced with permission [85]. Copyright 2018, London: Nature Publishing Group.

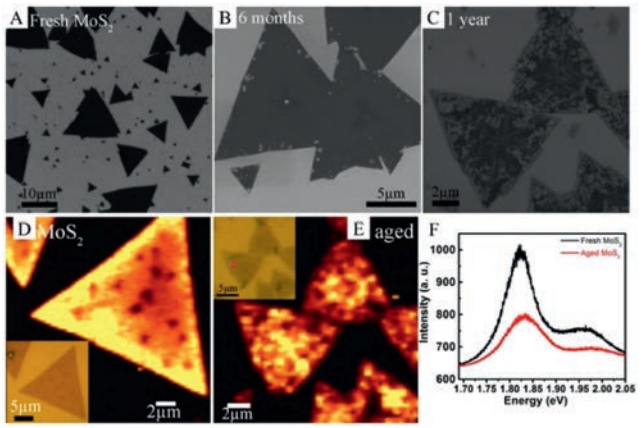

Fig. 4. Scanning electron microscopy images of (A) fresh MoS_2, and (B) aged MoS_2 after 6 months without desiccant and (C) after 1 year without desiccant. All the samples were stored in Class 100 cleanroom conditions. Photoluminescence spectra of fresh and aged TMDs. PL intensity map (centered at the A exciton) of fresh MoS_2 (D), and MoS_2 aged for 1 year under ambient conditions (E). The inset optical images show the MoS_2 flakes from which the data were taken. Representative PL spectra of the fresh and 1-year-aged MoS_2 (F). The 1 L MoS_2 films were aged for 1 year under ambient conditions (*i.e.*, room temperature and atmospheric pressure). Reproduced with permission [87]. Copyright 2016, American Chemical Society.

enthalpy of the final state is lower than for the initial state, drawing the conclusion that thermodynamically favorable for the S atoms to be removed from the MoS_2 basal plane through oxidation, namely, the oxidation of 1 L MoS_2 in the air is thermodynamically spontaneous. Nevertheless, resisted by the principle of kinetics, the substitutional oxidation of MoS_2 faces obstacle. The results of nudged elastic band model calculations (Fig. 3D) clarify that the typical kinetic barrier height is ~1 eV for the reaction pathway proposed. It is worth noting that along with the O substitution of the S vacancies, the energy of the final state was ~4 eV lower compared with the initial state, which clarifies that as a next step, the O substitution process is highly favorable.

In addition, in line with transition state theory, the dynamic obstacle of ~1 eV for the substitutional oxidation of MoS_2 are hopefully to be conquered in the room condition over a timescale of a month. The polarization curves (Fig. 3E) and corresponding Tafel plots (Fig. 3F) clarify that compared with the reduced pure 2D MoS_2 phase, the 2D $MoS_{2-x}O_x$ shows a dramatic increase in catalytic HER activity, which attributes to the single O atom incorporating into the MoS_2 basal plane progressively.

Furthermore, we may doubt if the substitution site is single O atom. As a matter of fact, taking O, O_2, OH saturated S vacancies into account, the only logical imagine, which was agreement with the experimental imagines is the single O atom substitution sites, which are also the thermodynamically most favorable case corresponding to −3.9 eV formation energy.

It is noteworthy that not all basal plane of TMDs can be spontaneously oxidized in air. The oxidation enthalpy of $MoSe_2$ basal plane to remove one Se atom by oxidation is $\Delta E = +0.75$ V, which means that it is thermodynamically unfavorable and difficult to spontaneously carry out the process of oxygen substitution of SVs. However, the edge oxidation speed of $MoSe_2$ is much faster than MoS_2, which means we cannot underrate overall environmental activity of $MoSe_2$. Namely, the spontaneous oxidation of $MoSe_2$ may still occur in different parts. Cucinotta *et al.* [86] reported the spontaneous oxidation process of TiS_2. In their research, the edge of TiS_2 is oxidized by water molecules as the function: $TiS_2 + xH_2O \rightarrow TiS_{2-x}O_x + xH_2S$. The open side of TiS_2 is more easily to be oxidized by water molecules. One of the H atoms is exchanged from water to a neighbor S-up atom, forming a thiol group, leaving a hydroxyl group adsorbed on Ti. In the next process, the H atom in a hydroxyl group moves to the opposite thiol group, forming the H_2S. The final configuration can be characterized by an O atom adsorbed at the edge, replacing one S atom. Actually, the spontaneous oxidation of TMDs could also be influenced by defects and edges. At the initial stage of spontaneous oxidation, the process is relatively slow relating to the intact MoS_2 basal plane. With the process of oxidation, dramatic defects are formed on the basal plane and the edges of TMDs are broken, which greatly speed up the subsequent oxidation process of TMDs. In the research of Gao *et al.* [87], they study on the spontaneous oxidation at the edges of MoS_2 and WS_2, and the oxidation process of the two is almost identical. Taking MoS_2 as the example (Fig. 4A), fresh 1 L MoS_2 synthesized using CVD had continuous smooth surfaces and were intact under the scale of 10 μm. After stored for 6 months without desiccant (Fig. 4B), it basically kept the original structure with little defects formed at the boundaries. However, after being oxidized at room temperature with desiccant for 1 year (Fig. 4C), the whole crystal was completely degraded and the defects were spread throughout the crystal face. Moreover, at the same time scale of the first six months and the second six months, it is obviously observed that the cracking in the second six months is more serious, which may indicate that when defects occur, the neighboring S atoms will be more easily oxidized, so the cracking speed will be faster.

Photoluminescence (PL) mapping and the optical image of a typical freshly grown 1 L MoS_2 is illustrated in Fig. 4D. Meanwhile, Fig. 4E shows the PL mapping of a typical MoS_2 oxidized for 1

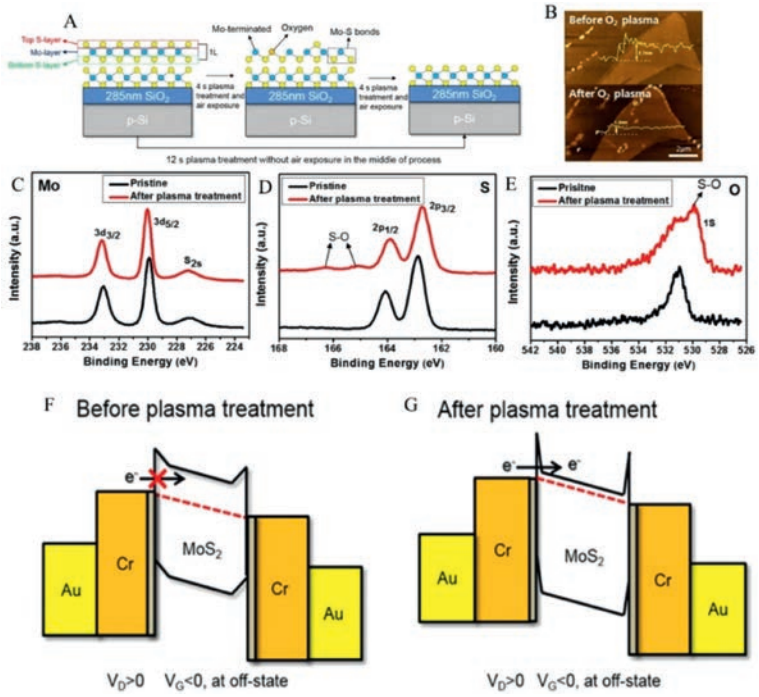

Fig. 5. (A) Illustrations for the atomic states of MoS_2 for showing atomic-level etching depending on the two different plasma treatment processes. (B) An AFM image before and after plasma etching. (C) Mo 3d, (D) S 2p and (E) O 1s XPS spectra of pristine MoS_2 and after plasma treatment. Schematic diagrams showing the structures and energy band diagrams of a MoS_2 FET Energy band diagrams at $V_D > 0$ and $V_G < 0$ (off-state) of MoS_2 (F) before and (G) after plasma treatment. Reproduced with permission [88]. Copyright 2016, IOP Publishing.

year. The PL spectrum of MoS_2 (Fig. 4F) is dominated by neutral A-exciton emission, along with B-exciton emission which results from the spin-orbital splitting of the valence band, ~0.15 eV away from the A peak. Obviously, compared with the preparation time, the PL intensity on the whole crystal surface of 1 L MoS_2 oxidized for 1 year changes greatly, and PL quenching occurs in some areas, which indicates that the surface of the sample has been greatly damaged by oxidation. The PL intensity of MoS_2 oxidized for one year is also reduced by 2.3 times (Fig. 4F) compared with the preparation time, which means that the composition of MoS_2 has changed dramatically after 1 year in the air, with most of the S atoms being replaced by O atoms. The above study shows that spontaneous oxidation in air can be very significant if the time is long enough.

3.1.2. Fabricated by oxygen plasma treatment

Oxygen plasma treatment is explored as the approach to controlling the band structure and thickness of the MoS_2 film, during which the S-O bonds are formed and enhance the character of MoS_2. Considering that if not regulated properly, the oxygen plasma treatment has the chance to oxidize MoS_2 to MoO_3, the low-intensity inductive coupled plasma (ICP) source should be used to minimize the chemical reaction. Comparing with traditional method, the MoS_2 treated by oxygen plasma treatment owns the advantage of smooth surface. Kim *et al.* [88] reported a precise process to prepare the 1 L MoS_2 with O atom doping (namely $MoS_{2-x}O_x$). The prepared few-layer MoS_2 films were transferred onto the Si/SiO_2 substrate. Before plasma treatment, the MoS_2 was cleaned through annealing at 250 °C for 3 h at Ar/H_2. Then, the precise regulation of MoS_2 layer was realized by generating an ICP discharge utilizing O_2 gas and varying treating time, a gas flow rate of 30 sccm, at a pressure of 200 mTorr, and a power of 21 W.

The mechanism of oxygen plasma treatment could be illustrated in Fig. 5A. The primitive MoS_2 was treated with the intervals of 4s. With air exposure, the Mo-S bonds are etched first, which produces abundant S vacancies. Afterwards, the O atoms replace the S vacancies, in which condition the S-O bonds are formed. As the AFM image shown in Fig. 5B, the thickness of 1 L MoS_2 has the 1 nm decrease, which may result from the oxidation or the absorption of H_2O in the air.

As we all know, the O_2 plasma is highly reactive and MoO_3, which is difficult to remove with high melting point of about 800 °C and insulative. The chemical reaction associated with the formation of MoO_3 is $2MoS_2 + 7O_2 \rightarrow 2MoO_3 + 4SO_2$. Therefore, it is significant to determine the existence of MoO_3. The X-ray photoelectron spectroscopy (XPS) analysis (Figs. 5C–E) clarified that compared with the primitive MoS_2, the MoS_2 treated after plasma treatment, only the Mo 3d peaks situated at 229.8 and 232.5 eV remain. Without observing the peak at 236 eV, the presence of MoO_3 could be excluded. Additionally, the peaks of 162.8 and 164.0 eV which are corresponded to S $2p_{3/2}$ and $2p_{1/2}$ and 529.8 eV corresponded to O 1s were observed, which provided the evidence of S-O bond formation. Therefore, by oxygen plasma treatment with restriction, the $MoS_{2-x}O_x$ nanosheet could be fabricated without the formation of MoO_3 nonconductor.

Similarly, Wang *et al.* [89] fabricated $WSe_{2-x}O_x$ by ultraviolet ozone and low power O_2 plasma treatment. They reveal that the oxygen plasma treatment on TMDs is an anisotropic process where the topmost layer is oxidized almost completely while the WSe_2 underneath are affected mildly. This phenomenon matches Fig. 5A well, which proves that most TMDs have similar characteristics.

In addition, it is crucial to restrict MoO_3 formation in oxygen plasma treatment. Meng *et al.* [90] reported that after plasma treatment, the PL lifetime of treated MoS_2 decreases from 494 ps to 190 ps due to the transformation to MoO_3, which illustrates the damage the MoO_3 deals to the character of $MoS_{2-x}O_x$ nanosheet. Furthermore, the plasma power should be limited. As reported by Lin *et al.* [60], when treated with strong power 100 W, the band gap of MoS_2 would be disordered, which is attributed to the amorphization of crystalline structure.

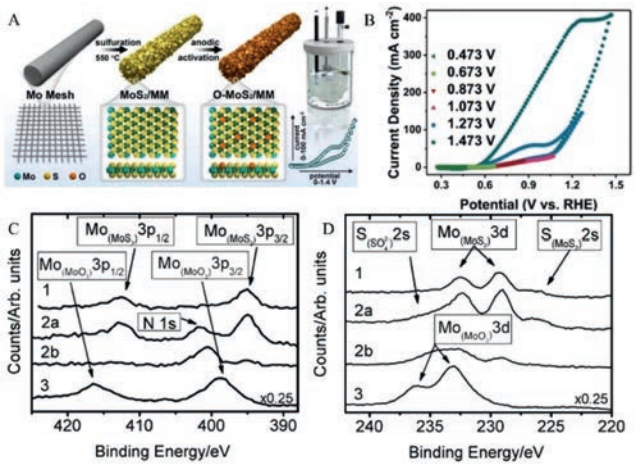

Fig. 6. (A) The synthesis of MoS_2/Mo mesh (MM), oxygen doped MoS_2/MM by anodic activation and the electrolyser and corresponding CV curve of anodic activation. (B) Cyclic voltammograms within the different range from +0.273 V to +1.473 V *vs.* RHE. Reproduced with permission [91]. Copyright 2019, Elsevier. (C, D) XPS spectra of MoS_2 on Toray paper recorded at different stages of its life. (1) As prepared after sulfidation. (2a) After initial activity measurements of the HER (CVs between +0.1 and 0.4 V *vs.* NHE). (2b) Sample 2a after measurements of the HER and subsequent oxidation/deactivation (CVs between +1.4 V and 0.4 V *vs.* NHE) and removal from the electrolyte at 0.32 V *vs.* NHE. (3) After measurements of the HER and subsequent oxidation/deactivation (CVs between +1.4 V and 0.4 V *vs.* NHE) and removal from the electrolyte at 0.4 V *vs.* NHE. Reproduced with permission [92]. Copyright 2009, The Royal Society of Chemistry.

To figure out the operating mechanism of the MoS_2 field effect transistors (FETs), the band diagrams before and after oxygen plasma treatment with a positive V_D and a negative V_G are shown in Figs. 5F and G. The primitive MoS_2 before plasma treatment shows off-state at negative V_G, which may result from the large barrier height between drain and source electrodes disturbing the electron flow. By contrast, the MoS_2 after plasma treatment did not show off-state, proving that the highly n-doped state, which is caused by oxygen atom doping, leading to the high field emission current in spite of the negative V_G. The oxygen plasma treatment could also improve the charge transport at contact interfaces. In the research of Wang *et al.* [89], it is evident by a 100–1000 times improvement in the p-type transport in WSe_2 FET, which means TMDs oxidized by oxygen plasma treatment have promising application prospects in FETs.

3.1.3. Fabricated by electrochemical methods

Electrochemical oxidation is also a fast and simple way to prepare MoS_2 with incorporation of oxygen. Usually, this process should be carried on in acidic environment. Deng *et al.* [91] reported that the MoS_2 is oxidized at the potentials above 0.65 V. The preparation process of oxidized MoS_2 they reported, which is representative in electrochemical oxidation, is shown in Fig. 6A. Firstly, the MoS_2 mesh (MM) was fabricated by the reaction of cleaned Mo mesh and S powder under the condition of 550 °C for 20 min. Furthermore, the prepared MoS_2 should be calcined at 350 °C with Ar with the intention to remove the excess S as possible. Finally, the MoS_2 mesh was implemented *via* cyclic voltammetry (CV) scans between +0.273 V *vs.* RHE and +1.273 V *vs.* RHE in 0.5 mol/L H_2SO_4 electrolyte by electrochemical oxidation for several cycles. In Fig. 6B, before the voltage increases to +0.873 V *vs.* RHE, the oxidation peaks of MoS_2 cannot be observed. As the applied voltage grows higher than +0.873 V, the current density increased with the cyclic voltammograms. In addition, the appeared hysteresis loop of CV curves proves the irreversible reaction from Mo^{4+} to Mo^{6+}, implying the incorporation of oxygen into MoS_2 which forms $MoS_{2-x}O_x$. In their research, the MoS_2 mesh with oxygen incorporation enhances the character of HER catalysts.

Meanwhile, the electrochemical oxidation of MoS_2 also exists in HER process. Bonde *et al.* [92] reported the change of MoS_2 composition (Figs. 6C and D). Through XPS spectra, compared with the primitive MoS_2 (No. 1), the MoS_2 tested for the HER (No. 2a) sweeping between +0.45 and −0.1 V *vs.* NHE only appears a peak of SO_4^{2-}, which is attributed to the H_2SO_4 condition. When the sweeping section enlarges which is between −0.4 V and +1.4 V *vs.* NHE (No. 2b), a significance reduction of the Mo 3d, Mo 3p, S 2s and S 2p peaks was observed. Nevertheless, the evidence which proves the existence of MoO_3 was not detected. Considering the sample 2b was pulled out of solution at −0.32 V *vs.* NHE, which may lead to the dissolution of MoO_3, the sample 3 was pulled out at +0.4 V *vs.* NHE. This time, the peaks corresponding to MoO_3 appear. The result conforms the theory mentioned above. In their research, the reaction was between two extreme conditions shown as equations as follows, which could be changed as the voltage and concentration of reactant:

$$MoS_2 + 11H_2O \rightarrow MoO_3 + 2SO_4^{2-} + 22H^+ + 18e^- \quad (1)$$

$$MoS_2 + 3H_2O \rightarrow MoO_3 + S_2^{2-} + 6H^+ + 4e^- \quad (2)$$

Thus, the HER catalyst contained with primitive MoS_2 may face the problem of oxidation. Fortunately, the pre-treatment of electrochemical oxidation of MoS_2 into $MoS_{2-x}O_x$ could handle this and enhance the catalytic performance, which avoid this dilemma. The research of Bonde *et al.* [92] also remind us that the electrochemical oxidation of MoS_2 should be carried out under restricted condition in avoid of the complete oxidation into MoO_3.

In summary, the TMD with O atom doping structure could be fabricated by various oxidation strategies. Notably, whatever the oxidation strategy is, it is significant to avoid the transformation of $MoS_{2-x}O_x$ into MoO_3. The formation of S-O bonds in $MoS_{2-x}O_x$ greatly enhance the chemical performance and this atomic structure could be widely used in applications of HER and FETs.

3.2. TMDs with oxygen bound up atop sulfur atoms

In some special circumstances, the O atom could absorb on top of sulfur, forming a unique atomic structure. It has been reported that the presence of ultraviolet light is indispensable to form this unique S-O bond [93,94]. This oxidation strategy could preserve the primitive MoS_2 structural and electronic properties as the formation of new S-O bonds.

Ultraviolet-ozone treatment provides a brand-new method to fabricate a special structure of oxidized MoS_2. Similar to other methods, the UV-O_3 treatment, as a way of strong oxidation, could transform MoS_2 into MoO_3, reported by Jung *et al.* [95]. In their research, the 1 L MoS_2 are treated by UV-O_3 for 5 min at the irradiance of 58 mW/cm^2. As illustrated in Figs. 7A and B, after 5-min UV-O_3 treatment, both the exfoliated flakes and CVD thin films of MoS_2 become transparent. As discussed above, this indicates that despite of the number of SVs, the MoS_2 could be oxidized to the transparent MoO_3 which conforms to the previous reports. The optical absorbance of MoS_2 thin films (Fig. 7C) clarifies that when the absorbance peaks of the primitive MoS_2 appears which attributes to excitonic transitions (A and B), the MoS_2 thin films treated by 5-min UV-O_3 exposure do not exhibit any peaks throughout the same range of the wavelength. Since light yellow-green MoS_2 thin films are transparent to visible light after 5 min UV-O_3 treatment, it is expected that the band gap of the original 1 L MoS_2 (~1.88 eV) becomes wider after UV-O_3 treatment. This is consistent with the wide band gap of MoO_3. UV-O_3-treated transparent MoS_2 indicates the formation of MoO_3 *via* 5-min UV-O_3 treatment.

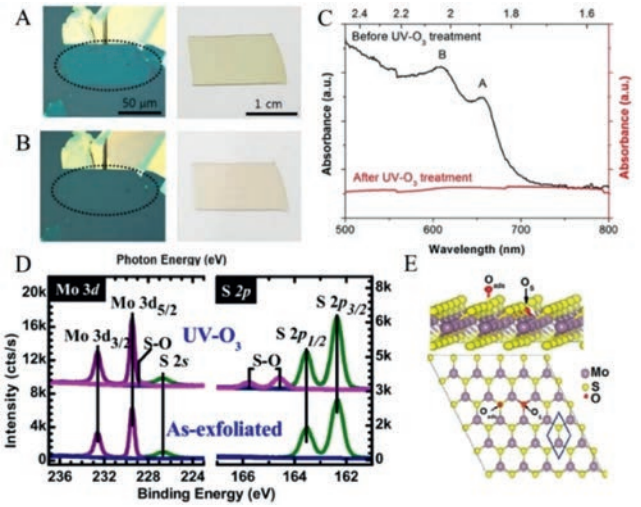

Fig. 7. Mechanically exfoliated flakes and CVD thin films of MoS_2 monolayers (A) before and (B) after 5-min UV-O_3 treatment (dotted region indicates monolayer). (C) Optical absorbance of CVD thin films before and after 5-min UV-O_3 treatment. Reproduced with permission [95]. Copyright 2019, Springer. (D) X-ray photoelectron spectra corresponding to the S 2p and Mo 3d (E) (5×5) supercell of MoS_2 showing the most energetically stable adsorption sites for oxygen: Oxygen on top of sulfur (O_{ads}) and substitutional oxygen on the SV (O_S). Reproduced with permission [96]. Copyright 2014, American Institute of Physics.

Notably, Azcatl *et al.* [96] reported that they found a non-destructive method to treat MoS_2 with UV-O_3 exposure without breaking Mo-S bonds, namely without the formation of MoO_3. The XPS spectra of MoS_2 treated in their research is given in Fig. 7D. Compared with the initial as-exfoliated MoS_2, the additional doublet peaks of the S 2p spectrum at 164.8 eV indicates the oxidation of sulfur. The increase of binding energy position of S 2p feature proves the sulfur is not the state of S^{2-} in MoS_2. However, the position is lower than that of S^{4+} reported previously. Considering the XPS spectra also illustrates that no formation of Mo-Mo and Mo-O bonds are detected, the oxidation of sulfur could be deduced as the formation of S-O bonds without the break of Mo-S bonds. The DFT modeling (Fig. 7E) clarifies that there are two different absorption sites of oxygen adatom: Oxygen atop sulfur and the substitution of SVs, which has the formation energies of −0.81 and −1.88 eV, respectively. The DFT result certifies that the formation of S-O bonds is energetically favorable which could occur without Mo-S scission. The result is in conformity with the states of Mo and S observed in XPS spectra. The MoS_2 has special structural characteristics different from other oxidized variants. The unique S-O bonds may arise some potential applications including atomic layer deposition [97] as reported. Huang *et al.* [66] also oxidized ReS_2 and $ReSe_2$ with UV light and got the O atom bound up atop S atom. Furthermore, they found that the formation of this structure is reversible. When the ReS_2 or $ReSe_2$ bound up atop O atom is exposure in laser, the oxidized ReS_2 or $ReSe_2$ could be transformed into the pristine ones. When studying on the transport properties of FET devices fabricated by ReS_2, they found that after UV treatment the on-state channel current drops by 1–2 orders of magnitude on average compared with the pristine ones. Considering that the reaction process is reversible, this property could be used to realize the switch of FETs under certain conditions.

4. Oxidized variants in the form of heterojunction

Obviously, the oxidation process of TMDs could be partially and locally, which forms the TMD-TMO (where TMO refers to transition metal oxides) heterojunction. Considering the heterojunction structure enhances the quantum effect and electron mobility of TMDs,

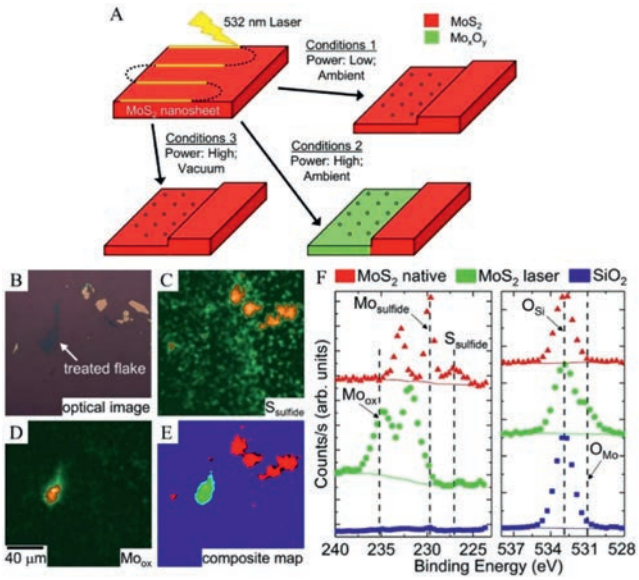

Fig. 8. (A) Laser-induced thinning conditions mostly result in nanoparticle formation (blue circles) on the MoS_2 surface, however different conditions impact surface chemistry. (1) Low-power laser and the presence of atmospheric oxygen retains the MoS_2 chemical structure. (2) High-power laser and the presence of atmospheric oxygen results in molybdenum oxidation. (3) High-power laser in the presence of vacuum also retains MoS_2 chemical structure. i-XPS measurements on native and laser-treated MoS_2 nanosheets treated in ambient conditions. (B) Optical image of the area containing native and laser-treated nanosheets. (C) Processed image attributed to $S_{sulfide}$ 2s signal. (D) Processed image attributed to Mo_{ox} 3d signal. (E) Composite map of masks associated with processed images of Mo_{ox} (green), $S_{sulfide}$ (red), and SiO_2 (blue) signals. Yellow, teal, and pink reflect an overlap in masks, while black reflects an absence in masks. (F) i-XPS spectra from the raw images based on pixels from the ROIs defined in the composite map. The Mo 3d and S 2s regions (left) and the O 1s region (right). Reproduced with permission [104]. Copyright 2018, American Chemical Society.

it is valuable to be prepared to apply in the fields such as field effect transistors [98,99], solar cells [100] and catalysts [101–103].

4.1. The bi-compound heterojunction

The bi-compound heterojunction is prepared with precise oxidation strategies and usually has the special shape. The unique shape of heterojunction may increase the active sites which improves the performance of products.

Laser-induced oxidation reaction is a directional, fast process with low activation energy and high selectivity. Considering the laser treatment could oxidize the TMDs locally and precisely which forms a straight channel, it is a useful method to prepare heterojunction of TMDs. Depending on this, Alrasheed *et al.* [104] investigated the theory of laser treating MoS_2 nanosheets. As shown in Fig. 8A, they treated the MoS_2 nanosheets on SiO_2 substrate with a 532-nm laser. Considering low laser power and ambient condition, the MoS_2 could not be oxidized lacking in energy, which gives rise to the amorphous MoS_2 etching and deposition upon the surface of the flakes. By contrast, when rising the laser power, the oxidized MoS_2 nanoparticles and nanosheets are able to be formed. Furthermore, as the removal of air, the nanosheet oxidation could not be observed. According to this mechanism, the oxidation of MoS_2 induced by laser could be influenced with circumstances including the laser power and the air condition. During i-XPS measurements, the optical images of native and laser treated MoS_2 are illustrated in Fig. 8B. When investigating the S 2s region at around 227 eV, the sulfur content of the native flakes remains which means the surface content is still MoS_2 (Fig. 8C). In the contrast, the region of treated flake grows dark, indicating the transformation of na-

tive MoS_2. When investigating the Mo 3d signal at 235 eV (Fig. 8D), only the treated flake is present, which proves the existence of oxidized MoS_2 (MoO_x). The masks of the $S_{sulfide}$, Mo_{ox}, and SiO_2 images with intention to identify regions of interest (ROIs) with minimal overlap resulting from masks were created from the $S_{sulfide}$, Mo_{ox}, and SiO_2 images to identify regions of the laser-treated and the native MoS_2 with the SiO_2 substrate is shown to extract spectra from the unprocessed images (Fig. 8E).

Spectra for the Mo 3d, S 2s, and O 1s regions which connect with pixels from each mask are offered in Fig. 8F. The native MoS_2 shows the typical Mo 3d and S 2s peaks at 229.8 eV and 227.0 eV respectively which is consistent with the literature value of MoS_2. Nevertheless, sulfur is nearly undetectable with slightly increases in signal intensity which is concluded in the satellite peaks for the shifted Mo 3d peak in the laser-treated MoS_2 flakes, suggesting that the characteristics of sulfide are completely removed. It is worth noting that the spectral features widen at half-width, indicating the presence of a distribution of oxide (Mo^{4+} to Mo^{6+}) species within the spectral envelope. However, in view of the binding energy of MoO_2 is close to that of MoS_2 and MoO_3 is usually found at locations where the binding energy is 0.5 eV to 1.0 eV higher, it is possible that an intermediate oxide component, such as Mo_2O_5, has been shown to be present near the observed fitting peak location.

Besides, adjusting the treating position of the laser, heterojunction with TMO in the middle of the TMD plane. Wang *et al.* [105] reported a novel type of lateral TMD-TMO heterostructure. In their research, the metallic NbS_2 as the "canvas" was etched by the laser heating. Due to the existence of oxygen in air, the 3R-NbS_2 with layered structure was oxidized to orthorhombic T-Nb_2O_5 locally, creating a patterned NbS_2-Nb_2O_5-NbS_2 heterostructure which has strong electrical signals in a two-terminal sensor resulting from its perfect interface contacts.

Thermal Annealing is a relatively simple form of oxidation modulation. Wu *et al.* [106] fabricated 1 L MoS_2 mesh by thinning the mechanically exfoliated multilayer MoS_2 nanosheets on SiO_2/Si substrates through thermal annealing in air. By means of this method, the above layers of MoS_2 nanosheets were etched, leaving only the bottom layer of MoS_2 with the existence of MoO_3 on the 1 L MoS_2. As illustrated in Figs. 9A–H, the optical images of exfoliated MoS_2 before and after annealing at different temperature ranging from 260 °C to 400 °C for 1 h clarified that when annealing at relative low temperature (at 260 and 300 °C), the MoS_2 nanosheets remained their primitive shape. As the temperature grows higher, multilayer MoS_2 nanosheets begin to get thinner (at 330 °C), and decomposed (at 400 °C) ultimately. Considering the general accepted fact that MoS_2 would oxidize completely to MoO_3, in their research, they chose 330 °C as the annealing temperature avoiding the complete decomposition of MoS_2 nanosheets.

It is worth noting that this preparation process is similar to the research of Zhou *et al.* [77] mentioned above. However, the reaction product is different. The reason of this phenomenon is that Zhou *et al.* carries out the heating process without the introduction of carrier or reactive gas, while Wu *et al.* prepares the chemical product in air which introduces abundant air. Another report from Yao *et al.* [107] expounds the mechanism of the heating progress. Due to the presence of oxygen, heating the MoS_2 sample in the air causes MoO_3 sites to appear on the surface. Due to the hydrophilicity of these MoO_3 sites, water molecules in the air are adsorbed to the surface of the sample, which further promotes the oxidation process. The same operation in a dry environment can prevent the adsorption of water molecules, making MoO_3 more volatile, so the degradation of MoS_2 in air is significantly slowed down. This report provides a reasonable excuse for the difference of the two researches mentioned above. By virtue of this, we conclude that the introduction of oxygen and water molecules could lead to the oxidation of MoS_2 into MoO_3 through the heating process.

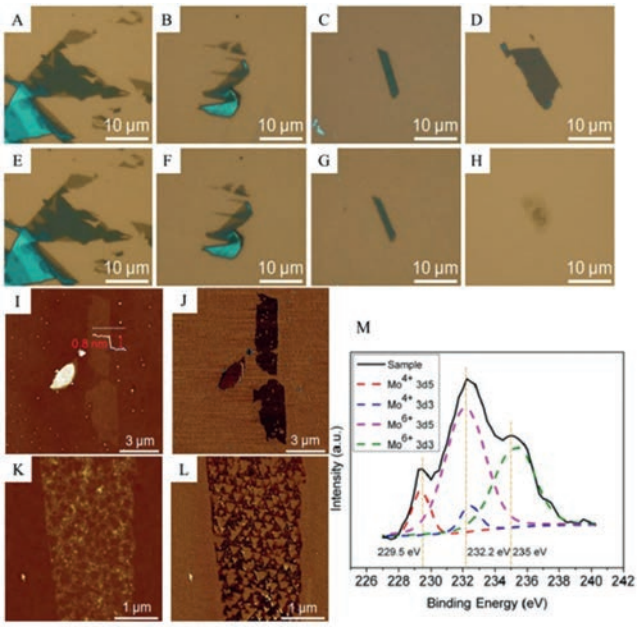

Fig. 9. Optical images of mechanically exfoliated MoS_2 nanosheets before (A-D) and after (E-H) thermal annealing in air for 1 h at 260 °C (E), 300 °C (F), 330 °C (G) and 400 °C (H). AFM height (I) and phase (J) images of MoS_2 nanosheet after thermal annealing for 10 h. AFM height (K) and phase (L) images of the MoS_2 nanosheet after thermal annealing for 15 h. (M) XPS spectrum of thermally annealed MoS_2 nanosheet. Reproduced with permission [106]. Copyright 2013, John Wiley & Sons, Ltd.

Taking the double-layer (2 L) MoS_2 into account, after annealing for 10 h, the 2 L MoS_2 nanosheet was thinned to 1 L. The AFM height and phase images (Figs. 9I and J) implied that the MoS_2 nanosheet annealed after 10 h has a smooth surface. It was worth noting that upon the relative smooth surface there existed small triangular pits with less than 200 nm size. Considering this, it was easy to suppose that if lengthening the annealing time, the pits may grow larger, in which case a MoS_2 mesh would form. As expected, when extending the annealing time to 15 h, the AFM height and phase images (Figs. 9K and L) showed the formation of MoS_2 mesh due to high density triangular pits resulting from the anisotropic etching. Notably, compared with MoS_2 nanosheet (Figs. 9K and L), the fabricated MoS_2 mesh owned a rougher surface, which arose from the more formation of MoO_3. As characterized by XPS (Fig. 9M), Mo 3d peaks at 232.2 eV and 235 eV, corresponding to Mo^{6+}, and Mo 3d peaks at 229.5 eV and 232.5 eV, corresponding to Mo^{4+}. Unifying with the practical situation, the Mo^{6+} are Mo^{4+} were contributed by MoO_3 and MoS_2 respectively. This result provided the evidence of the formation of MoO_3. In this way, the formation of triangular pits could be attributed to the evaporation of MoO_3. This research opened up a novel way to make MoS_2 mesh with MoO_3 doping.

The heterojunction with oxidation variants of TMDs could be used in some fields. For example, Almora *et al.* [108] reported that when heterojunction with oxidation variants like V_2O_5 and MoO_3 are made into solar cells, they have larger power conversion efficiency than before. And V_2O_5, due to its unique characteristics, is observed that flat solar cell architectures allow a significant increase in passivation of the heterojunction interface. The improvement has been supported by the exploration of the judge of minority carrier lifetimes and the depletion layer features. The more thorough understanding of heterojunction with TMD oxidized vari-

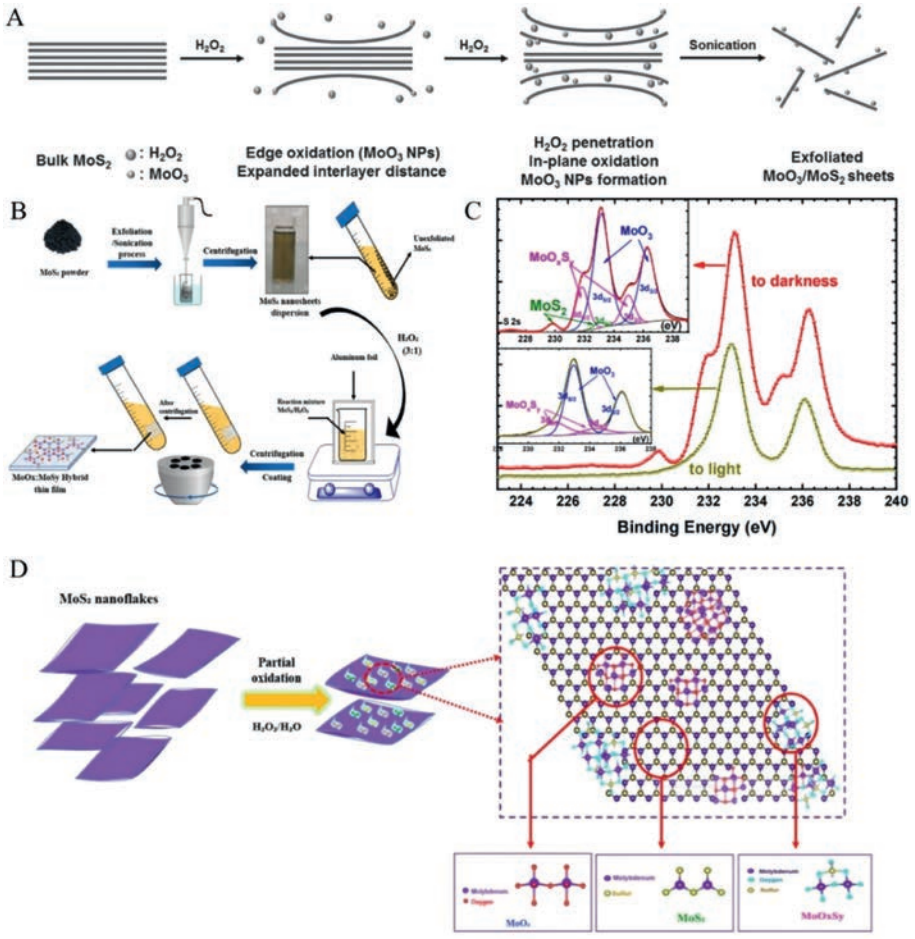

Fig. 10. (A) The schematic of exfoliation mechanism of MoO_3/MoS_2. Reproduced with permission [111]. Copyright 2014, John Wiley & Sons, Ltd. (B) Schematic illustration of MoS_2 exfoliation and hybrid thin film preparation by centrifugation-coating. (C) Mo 3d spectra of MoS_2 oxidized by H_2O_2 (10%) for 15 min to light and to darkness. (D) Illustration of the hybrid MoO_3:MoS_2 synthetic process, and the chemicals structure of MoO_3, MoS_2 and MoO_xS_y. Reproduced with permission [112]. Copyright 2022, Multidisciplinary Digital Publishing Institute.

ants could result in dramatic improvements for novel solar cells. As a matter of fact, the types of heterojunctions of TMD oxidized variants are myriad, and the structures and the combination of different compounds may produce different properties. Thus, there is still a long way to go to research on the fabrication of heterojunctions of TMD oxidized variants to explore more different types of applications.

4.2. The multi-compound heterojunction

In many cases, different oxides may be produced on the same TMD basal surface due to different oxidation sites and degrees [109,110]. Thus, some unique chemical properties may arise due to the wide variety of compounds. The reaction with H_2O_2 reagent is a typical method which produces a certain amount of MoS_xO_y in addition to MoO_3. There are also some special oxidized variants reported in few other reports, which confirm the multi-compound heterojunction with more oxidized variants could emerge.

As the reagent with strong oxidizing property, H_2O_2 is capable to transform MoS_2 into MoO_3. In light of this, to take H_2O_2 etching into multiple dimension application, we should add some limiting conditions in the process of reaction to decrease the oxidation rate in case of the MoS_2 decomposing to MoO_3 completely. As clarified in Fig. 10A, the mechanism of reaction of MoS_2, proposed by Yun *et al.* [111], could be described as follows: Firstly, due to the more highly active suspended bonds distributing at the edge of bulk MoS_2. As the process of oxidation, the interlayer distance of MoS_2 is expanded, which gives rise to the penetration of H_2O_2 into the expanded interlayer of MoS_2. Then, the interlayer of MoS_2 is partly oxidized to MoO_3. Meanwhile, the interlayer force gets weaker. Therefore, finally through ultrasound treatment, the atomically thin MoS_2/MoO_3 nanosheets can be prepared. The reaction allowed the equation:

$$MoS_2 + 9H_2O_2 \rightarrow MoO_3 + 7H_2O + 2H_2SO_4 \quad (3)$$

Lamkaouane *et al.* [112] reported that the oxidation rate of MoS_2 could be restricted under darkness condition. However, in most instances, there exists more than one kind of MoS_2 oxides. Lamkaouane *et al.* proposed a simple method to realize the theory. As illustrated in Fig. 10B, they exfoliated MoS_2 by liquid-phase exfoliation method in distilled water. Then, after a chain of centrifugation and stirring operation, they added H_2O_2 to the MoS_2 dispersion with a volume ratio of 3:1 at ambient temperature. After full of reaction, they transferred the MoO_3/MoS_2 to another centrifuge tube and obtained the MoO_3/MoS_2 thin film through another centrifugation process. As a matter of fact, they prove the existence of MoO_xS_y in the MoO_3 thin film.

As the XPS spectra shown in Fig. 10C, when using H_2O_2 with the concentration of 10%, after 15 min of oxidation at room conditions, the Mo 3d spectrum corresponds to two doublets: One situated at 232.9 eV and 236.0 eV results from the Mo $3d_{5/2}$ and Mo $3d_{3/2}$ of MoO_3. The other one situated at 231.7 eV and 234.8 eV corresponds to MoO_xS_y. It is obvious that no evidence shows the ex-

istence of MoS_2. According to the results, the MoS_2 is completely oxidized to MoO_3. In order to slow down the reaction, they tried to put the samples in the dark during the reaction. This time, after the same reaction time, the doublet situated at 229.0 eV and 233.0 eV appears, which proves the existence of primitive MoS_2. Fig. 10D illustrates the atomic structure of oxidized MoS_2. Due to the partial and different degrees of oxidation, the MoO_xS_y and MoO_3 could be detected in the MoS_2 nanoflakes. In summary, H_2O_2 owns the ability to oxidized MoS_2 to MoO_3 completely. With this method, H_2O_2 etching could be a straight way to prepare pure MoO_3. Meanwhile, to obtain the $MoO_xS_y-MoO_3-MoS_2$ heterojunction, the light condition and the concentration of H_2O_2 should be restricted.

In addition, in some reports, the researches gave the different reaction equations. For instance, Li *et al.* [113] gave the equation:

$$MoS_2 + 9H_2O_2 \rightarrow MoO_4^{2-} + 2SO_4^{2-} + 6H^+ + 6H_2O \quad (4)$$

However, Dong *et al.* [114] found that MoS_2 reacts with H_2O_2 under certain conditions through their own research:

$$MoS_2 + 9H_2O_2 \rightarrow MoO_2^{2+} + 2SO_4^{2-} + 2H^+ + 8H_2O \quad (5)$$

It can be seen that the specific reaction mechanism of MoS_2 and H_2O_2 is very complex, but one consensus could be drawn that the reaction of H_2O_2 and MoS_2 is violent, where a method to slow down the reaction must be taken.

In conclusion, the heterojunction structures could increase the recombination rate of electrons and holes and enlarge the width of the quantum well of the TMD atomic structure, which may enhance the luminous efficiency and electronic properties. As reported, the TMD heterostructures could be used in light-emitting diodes [115], photodetectors [116], solar cells [117], *etc.* Furthermore, considering the diversity of the heterojunction structures, endless application prospects are waiting to be explored.

5. Oxidized variants with uncommon structures

In addition to the various oxidative variant structures mentioned above, there are some more uncommon atomic structures. For example, $TiSe_2$ oxidizes in air, forming a special TiO_2 structure with Se atoms sandwiched between layers.

Sun *et al.* [118] reported a novel oxidation structure of metallic transition metal diselenides (Fig. 11A). In their research, the whole oxidation process was revealed as a layer-by-layer mode. Firstly, the topmost layer of $TiSe_2$ be oxidized spontaneously to $TiSe_{2-x}O_x$ in air condition, which has the similar atomic structure with $MoS_{2-x}O_x$ mentioned above. However, the $TiSe_{2-x}O_x$ is unstable in air. The further oxidation starts from the defects and edges which have high chemical activities. Then, the metastable Se-O-Ti bonds are broken gradually, in which circumstance selenium invades into the van der Waals gaps and accumulates into larger bulks which expand the interlayer distance and thus increase the overall height of the oxidized flakes. The enlarged gaps increase the contact area of O_2 and the multilayer flakes which attributes to the complete oxidation of the whole basal plane from top to bottom in the layer-by-layer formation. Finally, the $TiSe_2$ is oxidized to amorphous TiO_2 with Se nanoparticles inserted in the adjacent layers.

The Raman mapping images of $TiSe_2$ (Figs. 11B–D) as the time grows show the gradual oxidation process of $TiSe_2$. It is notably that the blue region becomes larger until it takes part of the whole basal plane, which indicates that the Raman active materials shifting from $TiSe_2$ to Se. Besides, the auger electron spectroscopy (AES) is utilized to characterize the elemental spatial distribution in the oxidized $TiSe_2$ flake (Figs. 11E–G). As the images illustrated, the Ti and O elements are homogeneously distributed in the oxidized $TiSe_2$ flakes, which indicates that the $TiSe_2$ is oxidized into TiO_2.

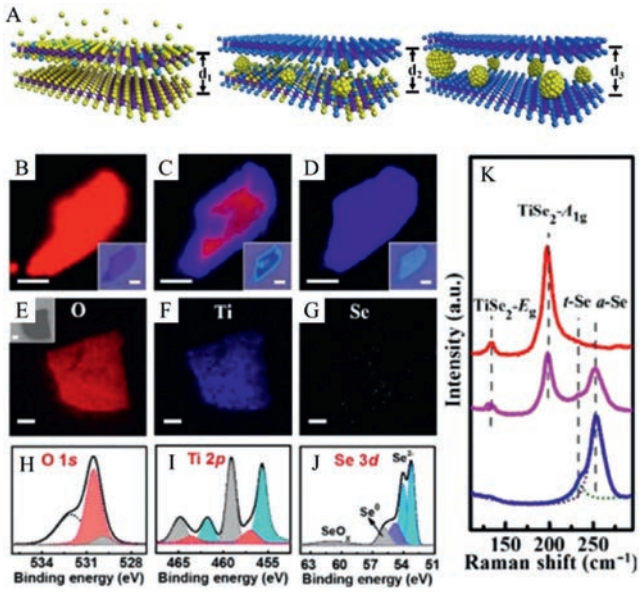

Fig. 11. (A) Schematics of the oxidation process of 2D $TiSe_2$. Evolution of $TiSe_2$ thin flakes in the progress of oxidation under ambient condition. Raman mapping images of (B) as-made $TiSe_2$ flake, (C) partially oxidized $TiSe_2$ flake after exposure to air for 5 days and (D) completely oxidized $TiSe_2$ flake after exposure to air for 10 days, respectively. Insets: corresponding optical images of $TiSe_2$ flakes. Scale bars: 1 μm. AES mapping images of (E) O, (F) Ti and (G) Se elements on the heavily oxidized $TiSe_2$ flakes. Scale bars: 2 μm. XPS spectra for binding energies of (H) O 1s, (I) Ti 2p and (J) Se 3d on the surface of partially oxidized sample, respectively. (K) Typical Raman spectra of as-made, partially oxidized and completely oxidized $TiSe_2$ flakes (from top to bottom), respectively. Reproduced with permission [118]. Copyright 2017, John Wiley and Sons.

Meanwhile, the amount of Se detected by AES is very low in the oxidized $TiSe_2$ flakes, clarifying that Se is stored deeper than the AES detection depth. To further confirm the elementary composition, the XPS spectra of the oxidized $TiSe_2$ is shown in Figs. 11H–J. The most prominent peak of O 1s locates at ~530–531 eV, which indicates the presence of Se-O-Ti bonds, besides the dominant O 1s peak caused by adsorption (~532 eV). Another small peak at ~529.9 eV is consistent with the O 1s binding energy of TiO_2. The doublet of Ti 2p at ~457.0 eV and ~463.6 eV also proves the existence of Se-O-Ti bonds in addition to those arisen by the primitive $TiSe_2$ and TiO_2. Furthermore, for Se 3d spectra, the peaks at ~54.8 eV and ~55.8 eV attribute to amorphous selenium and trigonal selenium, respectively, indicating the formation of Se elementary substance. Obviously, in the fully oxidized products, all Ti atoms exists in form of TiO_2 due to no signals of $TiSe_2$ and the intermediate are detected by XPS. The Raman spectra of partially oxidized and completely oxidized $TiSe_2$ (Fig. 11K) also shows that two new peaks appear at ~233 and ~253 cm^{-1} after oxidation, which belong to trigonal selenium and amorphous selenium respectively, and gradually replace the original peaks of $TiSe_2$. This also indicates that one of the oxidation products is selenium.

6. Applications of TMD oxidized variants

The TMDs have been widely used in different fields due to their tunable bandgaps and high catalytic activities. If the oxidation strategies mentioned are well utilized, the TMDs can be appropriately modified to enhance activities of basal plane and electronic transmission efficiency, thereby expanding the applications of TMDs. The typical applications of TMD oxidized variants are shown in Fig. 12.

(1) HER catalysts. Recently, the DFT calculation has proved that due to its proper hydrogen adsorption/desorption strength and

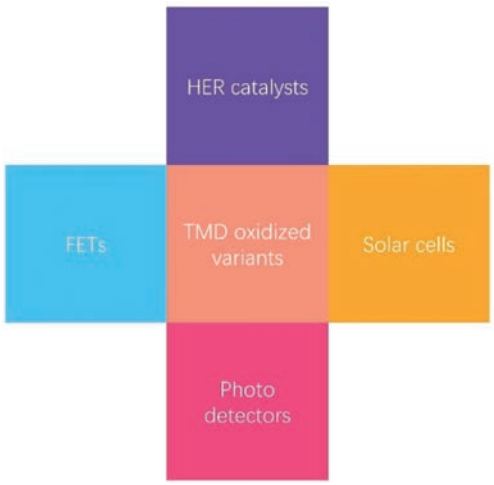

Fig. 12. The prospective applications of TMD oxidized variants summarized as examples.

good electrochemical stability [119–121], MoS_2 could be a promising HER catalyst if oxidation strategies are utilized to modify its low conductivity and increase active sites [122–126].

(2) FETs. With the improvement of device requirements, the sizes of transistors are becoming thinner. The silicon transistor has gradually failed to meet the requirement due to its physical limit. Meanwhile, TMDs are about to become promising candidate materials for the next generation of electronic devices due to their ultra-thin bodies and suitable bandgaps [127–129]. The excellent properties of TMDs are owing to their atomic nature and absence of dangling bonds. However, some doping strategies such as ion injection cannot be utilized in TMDs because they damage the atomic thin structure and the quality of devices [130]. Fortunately, oxygen plasma treatment can solve this problem because it allows the TMD to form a gapless band with removed S atoms [89,60], which reduces the contact resistance and provide a route for future device application.

(3) Solar cells. The TMD monolayers are potential materials to absorb sunlight and can be used to fabricate ultrathin photovoltaic devices due to their semiconductor properties. The researches have demonstrated that 1 nm thick active layers fabricated by TMD monolayers can obtain ~1% power conversion efficiency, which is about 1–3 orders of magnitude higher power density than the existing ultrathin solar cells [131,132]. When oxidation strategies are used to modify TMDs, the power conversion efficiency is better than before [108,117], which may arouse further studies on this field.

(4) Photodetectors. The vertical stacking of TMDs which forms van der Waals heterostructures has potential optoelectronic properties. This structure could realize efficient electron-hole separation and be applied in the fabrication of photodetectors [116,133,134]. Through modulation strategies, the low absorption capacity of TMD may be conquered and used in the detection of polarized light [135–137].

7. Conclusion and outlooks

As promising atomic structures, the oxidized variants have drawn extensive attention in recent years. Nowadays, plenty of researches have been carried out to comprehend the physicochemical properties of the structures and the fabrication methods. In the previous sections, we summarize the typical oxidation structures, including variants without changes of intrinsic elements, variants with single oxygen atom doping, heterojunction, and dioxides with interlayered elementary substance. By virtue of these results, the solid foundation of the further researches would be conducted and the wide application fields of TMD oxidized variants would be explored, such as HER catalysts, FETs and solar batteries. Although dramatic progress has been made, there still exist some obstacles and challenges worthy of further exploration.

(1) Although current studies have shown that precise TMD oxidation variants can be obtained through some specific ways, the preparation methods of some oxidation variants have strict requirements on reactants and reaction conditions. In these reactions, subtle changes in environmental conditions such as light and temperature may have an enormous impact on the oxidation products. Therefore, more stable and efficient preparation methods need to be explored in future research.

(2) In recent years, relevant researches have obtained many valuable oxidation variants through previous experience. It is still doubtful whether the structural types of oxidation variants can be expanded. The key to solving this problem lies in theoretical calculation. In the future research, we need to establish the relationship between the intrinsic properties and properties of materials at the atomic scale through theoretical calculations, and strive to efficiently find new materials with practical application value.

(3) At present, many kinds of TMD oxidation variants have been explored, but most of the researches on the specific properties of these oxidation variants still stay in the laboratory stage, and it is still unclear whether it can also be effective when it is applied to real life. In addition, there is still a long way to go from laboratory synthesis of oxidized variant materials to large-scale production, and more efforts are needed to promote the specific application of TMDs based oxidized variant materials.

Declaration of competing interest

The authors declare that they have no known competing financial interests or personal relationships that could have appeared to influence the work reported in this paper.

Acknowledgments

This work was financially supported by the National Natural Science of China (No. 51902101), Natural Science of Jiangsu Province (No. BK20201381), and Science of Nanjing University of Posts and Telecommunications (No. NY219144).

References

[1] Y. Wang, L. Zhou, M. Zhong, et al., Nano Res. 15 (2022) 3675–3694.
[2] G.H. Han, D.L. Duong, D.H. Keum, S.J. Yun, Y.H. Lee, Chem. Rev. 118 (2018) 6297–6336.
[3] Z. Sofer, D. Sedmidubský, J. Luxa, et al., Chem. Eur. J. 23 (2017) 10177–10186.
[4] C. Zhang, Y. Chen, A. Johnson, et al., Nano Lett. 15 (2015) 6494–6500.
[5] C. Ruppert, B. Aslan, T.F. Heinz, Nano Lett. 14 (2014) 6231–6236.
[6] F. Liu, J. Zhou, C. Zhu, Z. Liu, Adv. Funct. Mater. 27 (2017) 1602404.
[7] N.A. Pike, A. Dewandre, B. van Troeye, X. Gonze, M.J. Verstraete, Phys. Rev. Mater. 3 (2019) 074009.
[8] E. Malic, G. Berghäuser, M. Feierabend, A. Knorr, Ann. Phys. 529 (2017) 1700097.
[9] D. Nutting, G.A. Prando, M. Severijnen, et al., Nanoscale 13 (2021) 15853–15858.
[10] N.B. Shinde, B.D. Ryu, K. Meganathan, et al., ACS Appl. Nano Mater. 3 (2020) 7371–7376.
[11] C. Fan, T. Li, Z. Wei, et al., Nanoscale 6 (2014) 14652–14656.
[12] S. Wang, D. Zhang, B. Li, et al., Adv. Energy Mater. 8 (2018) 1801345.
[13] V. Caciuc, N. Atodiresei, S. Blügel, Phys. Rev. Mater. 2 (2018) 084001.
[14] D. Ma, W. Ju, T. Li, et al., Appl. Surf. Sci. 364 (2016) 181–189.
[15] H. Bai, Q. Wu, H. Ai, et al., Adv. Electron. Mater. 8 (2022) 2200209.
[16] G. Wu, Y. Ren, X. He, et al., Phys. Rev. Appl. 13 (2020) 024027.
[17] S. Imani Yengejeh, W. Wen, Y. Wang, Front. Phys. 16 (2020) 13502.
[18] N.K. Nepal, L. Yu, Q. Yan, A. Ruzsinszky, Phys. Rev. Mater. 3 (2019) 073601.
[19] D. Saleta Reig, S. Varghese, R. Farris, et al., Adv. Mater. 34 (2022) 2108352.
[20] N. Morell, A. Reserbat-Plantey, I. Tsioutsios, et al., Nano Lett. 16 (2016) 5102–5108.

[21] P. Jiang, X. Qian, X. Gu, R. Yang, Adv. Mater. 29 (2017) 1701068.
[22] D. Wang, X. Mu, W. Cai, et al., Compos. A: Appl. Sci. Manuf. 121 (2019) 36–44.
[23] G. Zhang, Y.W. Zhang, J. Mater. Chem. C 5 (2017) 7684–7698.
[24] I. Pallecchi, N. Manca, B. Patil, L. Pellegrino, D. Marré, Nano Futures 4 (2020) 032008.
[25] Q. Yun, L. Li, Z. Hu, et al., Adv. Mater. 32 (2020) 1903826.
[26] Q. Yun, Q. Lu, X. Zhang, C. Tan, H. Zhang, Angew. Chem. Int. Ed. 57 (2018) 626–646.
[27] X. Zhang, Z. Lai, Q. Ma, H. Zhang, Chem. Soc. Rev. 47 (2018) 3301–3338.
[28] L. Lin, P. Sherrell, Y. Liu, et al., Adv. Energy Mater. 10 (2020) 1903870.
[29] H. Huang, J. Zha, S. Li, C. Tan, Chin. Chem. Lett. 33 (2022) 163–176.
[30] T. Chowdhury, E.C. Sadler, T.J. Kempa, Chem. Rev. 120 (2020) 12563–12591.
[31] W. Cao, J. Kang, W. Liu, K. Banerjee, IEEE Trans. Electron Dev. 61 (2014) 4282–4290.
[32] J. Lindlau, M. Selig, A. Neumann, et al., Nat. Commun. 9 (2018) 2586.
[33] H. Lee, K. Lee, Y. Kim, et al., Nanoscale 11 (2019) 22118–22124.
[34] J. Ding, H. Zhao, X. Zhao, B. Xu, H. Yu, J. Mater. Chem. A 7 (2019) 13511–13521.
[35] M.V. Strikha, A.I. Kurchak, A.N. Morozovska, Phys. Rev. Appl. 13 (2020) 014040.
[36] H. Li, Y. Guo, W. Guo, Friction 10 (2022) 1851–1858.
[37] A. Rapuc, K. Simonovic, T. Huminiuc, A. Cavaleiro, T. Polcar, ACS Appl. Mater. Interfaces 12 (2020) 54191–54202.
[38] K. Chen, J. Pan, W. Yin, C. Ma, L. Wang, Chin. Chem. Lett. 34 (2023) 108226.
[39] X. Yang, B. Li, Nanophotonics 9 (2020) 1557–1577.
[40] S.L. Li, K. Tsukagoshi, E. Orgiu, P. Samorì, Chem. Soc. Rev. 45 (2016) 118–151.
[41] J.H. Park, S. Vishwanath, S. Wolf, et al., ACS Appl. Mater. Interfaces 9 (2017) 29255–29264.
[42] X. Cheng, L. Wang, L. Xie, et al., Chem. Eng. J. 439 (2022) 135757.
[43] S.S. Jo, A. Singh, L. Yang, et al., Nano Lett. 20 (2020) 8592–8599.
[44] Z. Luo, Y. Ouyang, H. Zhang, et al., Nat. Commun. 9 (2018) 2120.
[45] S. Kang, S. Kim, S. Jeon, et al., Nano Energy 58 (2019) 57–62.
[46] Q. Lu, Y. Yu, Q. Ma, B. Chen, H. Zhang, Adv. Mater. 28 (2016) 1917–1933.
[47] Y. Chen, Z. Liu, J. Li, et al., ACS Nano 14 (2020) 10258–10264.
[48] X. Hua, T. Axenie, M.N. Goldaraz, et al., ACS Appl. Mater. Interfaces 14 (2022) 2255–2262.
[49] S. Susarla, J.A. Hachtel, X. Yang, et al., Adv. Mater. 30 (2018) 1804218.
[50] X. Zhou, H. Hao, Y.J. Zhang, et al., Chem 7 (2021) 1626–1638.
[51] T. Wang, H. Zhu, J. Zhuo, et al., Anal. Chem. 85 (2013) 10289–10295.
[52] Y. Shu, L. Zhang, H. Cai, et al., Sens. Actuator. B: Chem. 311 (2020) 127863.
[53] T. Li, H. Li, J. Yuan, et al., Materials 15 (2022) 2654.
[54] M.Z.M. Nasir, Z. Sofer, M. Pumera, ChemElectroChem 2 (2015) 1713–1718.
[55] M. Ramya, P.S. Kumar, G. Rangasamy, et al., Environ. Res. 216 (2023) 114463.
[56] L. Yuwen, F. Xu, B. Xue, et al., Nanoscale 6 (2014) 5762–5769.
[57] K. Czerniak-Łosiewicz, M. Świniarski, A.P. Gertych, et al., ACS Appl. Mater. Interfaces 14 (2022) 33984–33992.
[58] P. Zhang, H. Xiang, L. Tao, et al., Nano Energy 57 (2019) 535–541.
[59] C.S. Pang, T.Y.T. Hung, A. Khosravi, et al., Adv. Electron. Mater. 6 (2020) 1901304.
[60] Y.C. Lin, B.M. Bersch, R. Addou, et al., Adv. Mater. Interfaces 7 (2020) 2000422.
[61] S. Park, S.Y. Kim, Y. Choi, et al., ACS Appl. Mater. Interfaces 8 (2016) 11189–11193.
[62] K.C. Kwon, C. Kim, Q.V. Le, et al., ACS Nano 9 (2015) 4146–4155.
[63] N. Papadopoulos, J.O. Island, S. Herre, G.A. Steele, IEEE Trans. Electron. Dev. 65 (2018) 4053–4058.
[64] H. Chen, X. He, Z. Zhou, et al., J. Nanobiotechnol. 20 (2022) 136.
[65] L. Yuwen, Y. Sun, G. Tan, et al., Nanoscale 10 (2018) 16711–16720.
[66] L. Huang, T. Yang, L.W. Wong, et al., Adv. Funct. Mater. 31 (2021) 2009166.
[67] X. Tan, W. Ding, Z. Jiang, L. Sun, Y. Huang, Nano Res. 15 (2022) 1973–1982.
[68] C. Zhang, D.F. Hu, J.W. Xu, et al., ACS Nano 12 (2018) 12347–12356.
[69] U. Maitra, U. Gupta, M. De, et al., Angew. Chem. Int. Ed. 52 (2013) 13057–13061.
[70] H. Jiang, D. Ren, H. Wang, et al., Adv. Mater. 27 (2015) 3687–3695.
[71] H. Jia, R. Yang, A.E. Nguyen, et al., Nanoscale 8 (2016) 10677–10685.
[72] X. Pan, M. Yan, C. Sun, et al., Adv. Funct. Mater. 31 (2021) 2007840.
[73] W. Yu, Z. Wang, X. Zhao, et al., Adv. Funct. Mater. 30 (2020) 2003057.
[74] S.X. Leong, C.C. Mayorga-Martinez, X. Chia, et al., ACS Appl. Mater. Interfaces 9 (2017) 26350–26356.
[75] Y. Li, X. Wang, F. Wang, Y. Tian, B. Yang, Vacuum 199 (2022) 110926.
[76] W. Li, J. Huang, B. Han, et al., Adv. Sci. 7 (2020) 2001080.
[77] H. Zhou, F. Yu, Y. Liu, et al., Nano Res. 6 (2013) 703–711.
[78] D. Lv, H. Wang, D. Zhu, et al., Sci. Bull. 62 (2017) 846–851.
[79] A. Syari'ati, S. Kumar, A. Zahid, et al., Chem. Commun. 55 (2019) 10384–10387.
[80] X. Ma, J. Zhang, Y. Sun, et al., ACS Appl. Mater. Interfaces 14 (2022) 47288–47299.
[81] A.W. Robertson, Y.C. Lin, S. Wang, et al., ACS Nano 10 (2016) 10227–10236.
[82] V. Paolucci, J. De Santis, V. Ricci, et al., ACS Sens. 7 (2022) 2058–2068.
[83] K. Czerniak-Łosiewicz, M. Świniarski, A.P. Gertych, et al., ACS Appl. Mater. Interfaces 14 (2022) 33984–33992.
[84] R. Ghosh, M. Singh, L.W. Chang, et al., ACS Nano 16 (2022) 5743–5751.
[85] J. Pető, T. Ollár, P. Vancsó, et al., Nat. Chem. 10 (2018) 1246–1251.
[86] C.S. Cucinotta, K. Dolui, H. Pettersson, et al., J. Phys. Chem. C 119 (2015) 15707–15715.
[87] J. Gao, B. Li, J. Tan, et al., ACS Nano 10 (2016) 2628–2635.
[88] S. Kim, M.S. Choi, D. Qu, et al., 2D Mater 3 (2016) 035002.
[89] J. Wang, X. Feng, D. Hedman, et al., Electrochem. Commun. 137 (2022) 107250.
[90] J. Meng, J. Zhu, S. Jia, X. Ren, Mater. Sci. 26 (2020) 143–146.
[91] Y. Deng, Z. Liu, A. Wang, et al., Nano Energy 62 (2019) 338–347.
[92] J. Bonde, P.G. Moses, T.F. Jaramillo, J.K. Nørskov, I. Chorkendorff, Faraday Discuss. 140 (2009) 219–231.
[93] K.M. Freedy, M.G. Sales, P.M. Litwin, et al., Appl. Surf. Sci. 478 (2019) 183–188.
[94] W. Zhang, T. Kanazawa, Y. Miyamoto, Appl. Phys. Express 12 (2019) 065005.
[95] C. Jung, H.I. Yang, W. Choi, Nanoscale Res. Lett. 14 (2019) 278.
[96] A. Azcatl, S. McDonnell, K. Santosh, et al., Appl. Phys. Lett. 104 (2014) 111601.
[97] H. Liu, K. Xu, X. Zhang, P.D. Ye, Appl. Phys. Lett. 100 (2012) 152115.
[98] W. Choi, J. Ahn, K.T. Kim, et al., Adv. Mater. 33 (2021) 2103079.
[99] J.Y. Lim, M. Kim, Y. Jeong, et al., npj 2D Mater. Appl. 2 (2018) 37.
[100] X. Yu, K. Sivula, Curr. Opin. Electrochem. 2 (2017) 97–103.
[101] A. Vijayan, N. Sandhyarani, J. Colloid Interface Sci. 623 (2022) 819–831.
[102] S. Seo, S. Kim, H. Choi, et al., Adv. Sci. 6 (2019) 1900301.
[103] H.T.T. Nguyen, L.A. Adofo, S.H. Yang, et al., Adv. Funct. Mater. 33 (2023) 2209572.
[104] A. Alrasheed, J.M. Gorham, B.C. Tran Khac, et al., ACS Appl. Mater. Interfaces 10 (2018) 18104–18112.
[105] B. Wang, H. Luo, X. Wang, et al., Nano Res. 13 (2020) 2035–2043.
[106] J. Wu, H. Li, Z. Yin, et al., Small 9 (2013) 3314–3319.
[107] K. Yao, J.D. Femi-Oyetoro, S. Yao, et al., 2D Mater 7 (2019) 015024.
[108] O. Almora, L.G. Gerling, C. Voz, et al., Sol. Energy Mater. Sol. Cells 168 (2017) 221–226.
[109] K. Kang, K. Godin, Y.D. Kim, et al., Adv. Mater. 29 (2017) 1603898.
[110] H. Li, J. Wu, Z. Yin, H. Zhang, Acc. Chem. Res. 47 (2014) 1067–1075.
[111] J.M. Yun, Y.J. Noh, C.H. Lee, et al., Small 10 (2014) 2309.
[112] H. Lamkaouane, H. Ftouhi, M. Richard-Plouet, et al., Nanomaterials 12 (2022) 3071.
[113] Q. Li, B. Hu, Q. Yang, et al., Environ. Res. 191 (2020) 110227.
[114] L. Dong, S. Lin, L. Yang, et al., Chem. Commun. 50 (2014) 15936–15939.
[115] F. Withers, O. Del Pozo-Zamudio, A. Mishchenko, et al., Nat. Mater. 14 (2015) 301–306.
[116] M. Massicotte, P. Schmidt, F. Vialla, et al., Nat. Nanotechnol. 11 (2016) 42–46.
[117] N.R. Paudel, C. Xiao, Y. Yan, Prog. Photovolt. 23 (2015) 437–442.
[118] L. Sun, C. Chen, Q. Zhang, et al., Angew. Chem. Int. Ed. 56 (2017) 8981–8985.
[119] T.F. Jaramillo, K.P. Jørgensen, J. Bonde, et al., Science 317 (2007) 100–102.
[120] H. Wang, X. Xiao, S. Liu, et al., J. Am. Chem. Soc. 141 (2019) 18578–18584.
[121] W. Yin, L. Yuan, H. Huang, et al., Chin. Chem. Lett. 35 (2024) 108351.
[122] D. Yan, C. Mebrahtu, S. Wang, et al., Angew. Chem. Int. Ed. 62 (2023) e202214333.
[123] D. Yan, C. Xia, W. Zhang, et al., Adv. Energy Mater. 12 (2022) 2202317.
[124] P. Fan, Y. He, J. Pan, et al., Chin. Chem. Lett. 35 (2024) 108513.
[125] C. Chang, L. Wang, L. Xie, et al., Nano Res. 15 (2022) 8613–8635.
[126] M. Liu, H. Li, S. Liu, et al., Nano Res. 15 (2022) 5946–5952.
[127] Y. Sheng, L. Zhang, F. Li, et al., J. Mater. Sci. Technol. 69 (2021) 15–19.
[128] M. Wang, W. Wang, Y. Zhang, et al., Chin. Chem. Lett. 32 (2021) 3118–3122.
[129] J. Li, J. Pan, W. Yin, et al., Chin. Chem. Lett. 34 (2023) 108049.
[130] K. Xu, Y. Zhao, Z. Lin, et al., Semiconduct. Sci. Technol. 32 (2017) 124002.
[131] M. Bernardi, M. Palummo, J.C. Grossman, Nano Lett. 13 (2013) 3664–3670.
[132] M. Li, L. Wang, X. Zhang, et al., Chin. Chem. Lett. 34 (2023) 107775.
[133] J. Yan, X. Yang, X. Liu, et al., Adv. Sci. 10 (2023) 2207022.
[134] T. Shen, F. Li, Z. Zhang, L. Xu, J. Qi, ACS Appl. Mater. Interfaces 12 (2020) 54927–54935.
[135] B. Xu, H. Shen, Y. Xu, et al., J. Alloys Compd. 874 (2021) 159864.
[136] Y. Fu, Y. Liu, K. Ma, et al., J. Alloys Compd. 819 (2020) 153063.
[137] Z. Li, Z. Hu, J. Peng, et al., Adv. Funct. Mater. 24 (2014) 1821–1830.